

Chapter 5

Al-Mg alloy thin films on Si(111)

An alloy is a liquid or solid solution of two or more elements. The structure of alloys varies, depending on their composition, temperature, pressure and forming elements. In the simplest case the elements are completely soluble and present a continuous variation of the structure with composition. However, this is not generally the case: usually the solubility is only partial. A particularly convenient way to represent the variation of the structure with the relative composition of the alloys is the phase diagram, where the different *phases*, i.e. domains of homogeneous concentration and structure, are presented in a temperature (or pressure) vs. concentration diagram. The simplest phase diagrams are those of completely soluble alloys, while the partially soluble systems are characterized by more complex phase diagrams, with transitions between different structures and coexistence of phases. Among the partially soluble alloys, the eutectic alloys, which are completely soluble in the liquid state but not in the solid state, are very important. Solidification of an eutectic alloy from the liquid phase produces two composite solid phases characterized by different solute concentrations. It is possible also for eutectic alloys to solidify into single phase compounds, but this happens only at certain particular compositions. Consider the phase diagram of the Al-Mg system shown in figure 5.1. The phases defined by

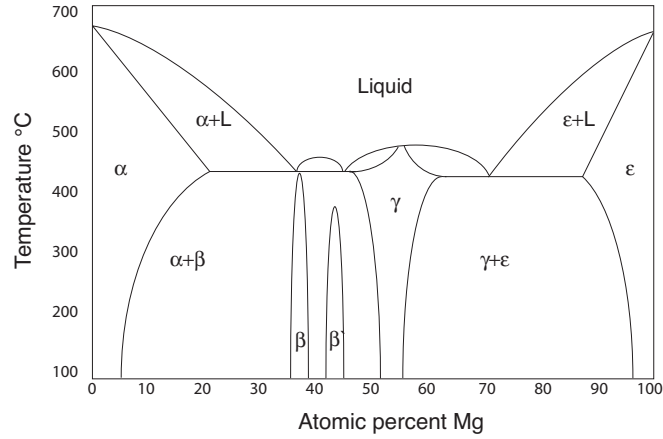


Figure 5.1: Phase diagram of the Al-Mg alloy system.

β , β' and γ , represent three intermetallic compounds, namely the Mg_2Al_3 ¹ and the $\text{Al}_{12}\text{Mg}_{17}$. The α and ϵ phases are the pure Al and Mg.

The binary alloys obtained by solution of simple metals are technologically very important materials, especially due to their mechanical properties, but they are also interesting from a more fundamental point of view, because the relative simplicity of the band structure of the forming elements can be tailored in the binary system.

The Al-Mg alloys present similar features to other binary alloys, such as an excellent strength to weight ratio, good ductility and corrosion resistance, making them widely used in the mechanical industry.

However, one more peculiarity of the Al-Mg system is the close similarity of their structure with many quasicrystals. Therefore the electronic properties of such systems can be of great importance in the study of the more complex quasicrystals obtained by alloying Al, Mg and a small amount of a transition metal or another simple metal (examples are the Al-Mg-Zn and the Al-Mg-Li alloys). Moreover, an interesting Al doping behaviour has been observed in the recently discovered high T_c superconductor MgB_2 doped with Al [60]. The resulting material $\text{Al}_x\text{Mg}_{1-x}\text{B}_2$ shows a dependence of T_c on the quan-

¹The difference between the β and β' phases is in the order and the extension of the unit cell, in fact, the former has a complex fcc structure with a lattice constant of about 28 Å and about 1100 atoms in the unit cell and the latter has an hexagonal structure with lattice parameters $a=10.02$ Å and $c=16.36$ Å.

tity x of doping Al [61]. From a theoretical point of view, *ab initio* virtual crystal approximation (VCA) calculations [62] demonstrated that electronic doping due to Al introduction raises the Fermi level to higher energies, leading to a band broadening and to a continuous variation of lattice constant with x , as result of the different Wigner-Seitz radius of Mg and Al.

5.1 Simple metals and binary alloys

A characteristic of the s-p metals is the simplicity of their electronic structure, which is essentially the s-p derived nearly free electron (NFE) band. This property determines the great mobility of the electrons which can move almost freely in the medium represented by the periodic ionic potential. Thin films of sp-metals are very interesting to study because their properties are strongly dependent on the size of the films, and in particular they can induce a discretization of the s-p band due to the confinement of the electrons in a 2D potential well. Because of the simplicity of the theoretical model, quantum size effects in s-p metals have been intensively studied and several thin film electronic structure calculations are available [63]. Aluminum and magnesium are two examples of s-p metals, and indeed many theoretical studies refer to them, although the experimental observation of quantum well states (QWS) for thin films of aluminum and magnesium has been published only very recently [64],[65].

Aluminum crystallizes in the face centered cubic structure (fcc) with lattice constant of 4.05 Å. The corresponding reciprocal lattice is body centered cubic, with the first Brillouin zone represented in Fig. 5.2. Magnesium has a hexagonal close packed (hcp) structure with lattice constants $a=3.19$ Å and $c=5.18$ Å, thus with an almost ideal c/a ratio for a close packed structure. The Brillouin zone for Mg is shown in Fig.5.2 as well. The electronic structure of Al(111) and Mg(0001) in the direction of interest for our study are shown in Fig. 5.3. The NFE band extends over a large energy region and for both metals a gap is present, due to the Bragg reflection of the wavefunction at the Brillouin zone boundary. Within this gap, a Shockley-type surface state has been predicted for both elements and, indeed, experimentally observed: at about 4.7 eV for Al(111) [66], and at about 1.7 eV for Mg(0001) [67].

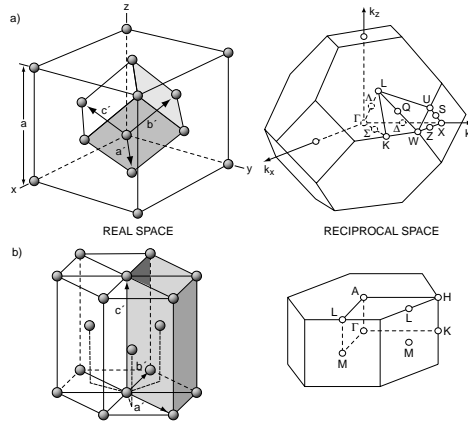


Figure 5.2: Unit cell and first Brillouin zone of a fcc (a) and a hcp (b) crystal.

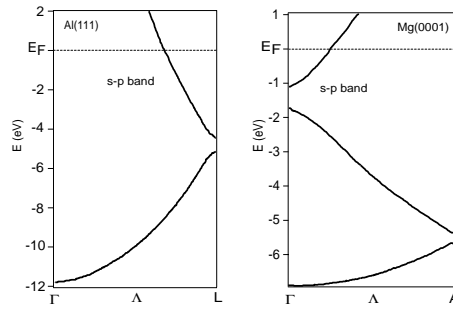


Figure 5.3: band structures of Al(111) and Mg(0001) in the direction of interest for confinement.

5.1.1 Binary alloys

The way a binary alloy behaves depends on the relative concentrations of the alloy components and on the electronic and atomic properties of both components in a complex way. Apart from the ordered compounds, a peculiarity of all the alloys is the loss of long-range periodicity leading to the inapplicability of Bloch's theorem, at least in its direct formulation. However, the observation in the last decades of bulk and surface bands in systems with no translational symmetry, shows that the band picture can be modified to be applied to such systems [68].

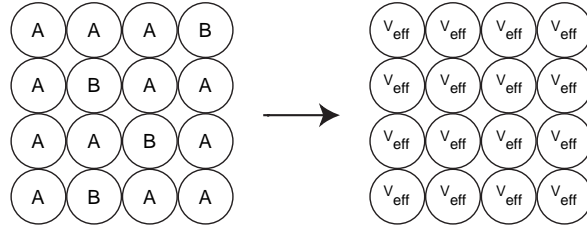


Figure 5.4: Schematic illustration of the restoring of crystalline order with the introduction of effective atoms. This theory is known as virtual crystal approximation (VCA).

The effect of alloying of two metals consists in the variation of various properties: the lattice constant and the stable crystalline structure; the charge density \mathbf{n} on which the Fermi energy E_F , the Fermi wave vector k_F , the radius r_S of the sphere which contains on average one electron, the work function Φ and the potential V , depend. The different theories concerning the formation of alloys take care of all these effects in various ways depending on the approach to the problem.

In order to tailor the powerful Bloch theorem to systems with no long range order, it is possible to substitute the disordered crystal with an ordered one formed by atoms with averaged parameters depending on the composition of the system. In such a way, the order is restored and it is in principle possible to study the average properties of the disordered crystal with the same mathematical tools used for studying the ordered systems (see Fig. 5.4).

The way the disordered crystal is approximated with an effective ordered one can be formulated in various manners: two of these are the virtual crystal approximation (VCA) and the coherent potential approximation (CPA). In the former one, the potentials V_A and V_B of the two different ions A and B are substituted by one effective potential, just by considering $V(c) = V_A(c) + V_B(1 - c)$ where c is the concentration of element A in the alloy. The approach of the CPA is instead related to the scattering of the electrons, which is considered to be caused by the effective potential. In this case, the two different potentials are substituted by one which scatters in an effective way and, apart from this effective scattering, there are no further single-site scattering events.

The VCA approximation is an extension of a simple model proposed by

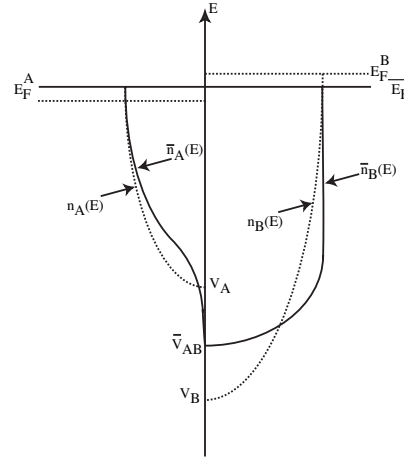


Figure 5.5: Model used by Schlüter and Varma to explain the changes due to alloying of two materials with different electronic properties [71].

Jones already in 1934 and called *rigid band model* [69], in which in the case of elements with similar band structure but different bandwidth, the alloying process results in a band structure similar to the two and with a bandwidth depending only on the relative concentration of the two elements. Hence, the valence band is rigidly shifted with respect to the Fermi edge by changing the composition. This result is indeed obtained also in the VCA model, but with the difference that a density of states profile dependence on the alloy composition is also taken into account, meaning that the alloying process is characterized also by a charge transfer.

Neddermeyer [70] studied the Al-Mg alloy system by means of X-ray emission, and found that the bandwidth of the Al and Mg $K\beta$ bands have the same common value lying between those of the pure elements, while he could not gain any direct information about the density of states of both components, which would confirm the basic idea of the rigid band model of Jones. In order to understand how the density of states profile enters into the alloy process, a very intuitive approach to the VCA approximation has been proposed by Schlüter and Varma [71], who used a simple model based on the essential physics to calculate the stability of many binary alloys of simple metals.

Their idea was that, starting from two s-p metals A and B with local density of states per unit volume $n_A(E)$ and $n_B(E)$ which are zero below the potentials V_A and V_B , respectively, the alloy formation will result in an averaged local density of states $\bar{n}_A(E)$ and $\bar{n}_B(E)$. They calculated in a self-consistent

way the mean potential associated with the redistribution of the charge obtaining an averaged \bar{V}_{AB} . If, for example, $V_A < V_B$, the potential of element B will reduce to the averaged potential accumulating electrons, coming from element A, at the bottom of the spectrum, arriving at the situation depicted in Fig. 5.5. This model predicts thus an averaged, common Fermi level, dependent on the composition of the alloy.

The other approach, which makes use of the CPA approximation, has been proposed by Bansil and Pessa [68] who used this approximation more specifically to explain their photoemission results in $\text{Cu}_x\text{Al}_{1-x}$ alloys. In these alloys they observed the existence of both Tamm and Shockley-type surface states derived from the respective surface states of Cu, where the Shockley surface state on the (111) and (110) faces shifted by varying the Al concentration of the alloy, while the Tamm-type surface states on the (100) and (111) surface did not.

The CPA theory predicts that the location, in a disordered way, of Al atoms in the Cu lattice sites produces bulk wave functions with k values with an imaginary component, resulting in the broadening of the electronic bulk bands and eventually in the shift of the gap position and of the surface state, with influences on the bandwidth given only by the broadening of the bands. The difference of behaviour between the Shockley and the Tamm state is given by their different nature: while the Tamm states are thought to be split off from the top of the Cu d -bands, the Shockley states are positioned in the gap which arises from the mixing of the states possessing s - p character, so the movements of the surface states on alloying follow those of the bulk states of corresponding symmetry [68].

The reason why the CPA was used in the study of Bansil and Pessa is because it is more useful in treating the Cu d -bands. But, nevertheless, the result that only the gap position with respect to the Fermi edge influences the surface state energy, and therefore, only the Shockley-type surface states are influenced by the alloy composition, shows that the VCA approximation can be used as well. Indeed, we have also to note that in our case of AlMg alloys there are no d -bands involved, so the comparison between our system and that of Bansil and Pessa has to take into account this substantial difference.

Except for some experimental studies done with Auger spectroscopy [72] aimed at studying the mechanical properties of the Al-Mg alloy and in par-

ticular Mg segregation, the only experimental study of the electronic properties of these alloys is the above cited X-ray emission work reported by Neddermeyer [70]. Photoemission is a very powerful tool for studying the electronic structure of the bulk and surface of solids, it is therefore very important to use this technique also for these systems and in particular for thin films of Al-Mg alloys to obtain more knowledge of the alloying process.

5.2 Photoemission and QWS

The simplest way to understand the formation of QWS is the 1D model of the “particle-in-a-box” where the electron is confined by two infinite barriers at a distance comparable with the particle wavelength, causing the discretization (quantization) of the energy values. The adaptation to the case of a thin film of thickness d is made through the 1D phase accumulation model [73],[74]. Here the electrons of the film are confined in the direction perpendicular to the surface by the image potential at the surface of the metal, and by the energy gap in the substrate, resulting in a reflection of the electron on both walls with a changing of the phase Φ of the electron wave function Ψ . In this direction the wave vector values k are allowed only if they fulfill the condition:

$$2kd + \Phi_B + \Phi_C = 2\pi n \quad (5.1)$$

stating that the round trip phase accumulation of the electrons must be a multiple of 2π , similarly to the condition of constructive interference in the Bohr atomic model for a complete turnaround the atomic nucleus. Here Φ_B is considered the phase shift at the vacuum barrier and Φ_C the shift at the crystal substrate gap.

The determination of Φ_B and the Φ_C as a function of binding energy E is a very important and indeed very complicated task. A useful approximation for the reflection phase shift at the surface is given by [75]:

$$\Phi_B = \pi \sqrt{\frac{3.4eV}{E_V - E}} - \pi \quad (5.2)$$

where E_V is the vacuum level, while for the phase shift at the interface there is an empirical formula which gives [73]:

$$\Phi_C = 2 \arcsin \sqrt{\frac{E - E_L}{E_U - E_L}} - \pi \quad (5.3)$$

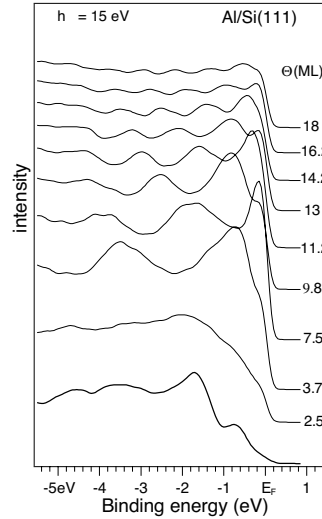


Figure 5.6: Photoemission spectra taken at 15 eV photon energy for various film thicknesses of Al/Si(111). The substrate temperature during Al deposition was about 100K. The spectra were taken after annealing at 200K.

where E_L and E_U are the energies for the lower and the upper parts of the band gap in the crystal substrate.

The consequence of equation (5.1) is that the states for which the energy falls within the range of the gap in the surface projected band structure of the substrate are discrete. The band gap at the interface does not necessarily have to be an absolute gap, but may also be a symmetry-induced gap or maybe caused by a break in lateral symmetry due to lattice mismatch between the substrate and the overlayer thus causing a higher reflectivity. The effect of confinement is particularly clear in regions of the band structure where a NFE band is present, such as the s-p band of the simple metals Mg and Al (see Fig. 5.3): the quantization of the k values due to the reduced size of the thin film results in a split of the NFE bands into discrete energy values. In the energy distribution curves (EDC) obtained in photoemission, the quantization of energy values leads to separate peaks. In the case of Mg and Al the situation is advantageous because for a large range of binding energies, only the s-p bands are present, making the interpretation of the photoemission spectra simpler.

In Fig. 5.6 we show photoemission spectra from the Al/Si(111) system. With increasing Al film thickness, there is an increase of the number of peaks and a shift of their binding energy as expected since the well is getting wider. From (5.1), it is possible to obtain the equation of k for the allowed

normal wave vector values of the film:

$$k = \frac{n}{N} \cdot \frac{\pi}{a} - \frac{1}{N} \frac{\Phi_B + \Phi_C}{2a}, \quad (5.4)$$

where the thickness d of the film has been substituted by the number of layers N times the interatomic distance a . Another useful way to describe the QWS is the equation

$$k = \left(1 - \frac{m}{N}\right) \cdot \frac{\pi}{a} - \frac{1}{N} \frac{\Phi_B + \Phi_C}{2a}, \quad (5.5)$$

where the reduced quantum number $m = N - n$ has been introduced. With this definition the state with $m = 1$ is always the closest to the valence band maximum and maintains its number m as the thickness increases.

Increasing the number of layers, the value of k determined by equation (5.4) changes, leading to a shift of binding energy. At some point a new state crosses the E_F and a new peak is observed in the photoemission spectrum. The relation between the number of QWS and the thickness is given by the point where the bulk s-p band cuts: for example in the case of Al in $\Gamma - \mathbf{L}$ direction, there is a crossing of E_F at 1/3 of the Brillouin Zone (BZ), so a new QWS will cross E_F every 3 ML.

5.3 Experimental setup

The experiments were performed at BESSY on the beamlines 3m-NIM and TGM-4. These beamlines, located on bending magnets, have monochromators that offer the possibility to measure in the 5-30 eV range on the 3m-NIM and in the range 8-130 eV on the TGM-4, with a good energy resolution of ~ 30 meV and a photon flux of $\sim 10^{11}$ photons/s. The use of low photon energy was decisive for obtaining good results, since, as will be shown later, in the range 10-15 eV the valence band cross-section has a huge enhancement due to collective electron excitations.

The vacuum system used in these experiments was equipped with an ADES 400 hemispherical electron energy analyzer with a nominal radius of 50 mm and an angular acceptance of 1.5° . The estimate total energy resolution, determined by the width of the Fermi edge, was about 50 meV in the photon energy range used.

The vacuum chamber was also equipped with low energy electron diffraction

(LEED) for checking the periodicity of the clean surface of the Si substrate and of the thin films. The samples were cut from a commercial Si(111) wafer, p-type doping (B), $0.5 \Omega\text{cm}$ resistivity (Virginia Semiconductors). The samples mounted on the manipulator could be degassed, annealed and flashed by direct resistive heating and cooled to liquid nitrogen (LN_2) temperature through a cold finger. To produce clean Si(111) surfaces, the samples were first degassed at $\sim 650^\circ\text{C}$ for several hours and then flashed at $\sim 1200^\circ\text{C}$, while the manipulator was cooled with LN_2 . The pressure burst during the flash was maintained in the 10^{-10} mbar range. The samples were then quickly cooled to $\sim 900^\circ\text{C}$ and then further cooled to low temperature within some minutes. The procedure ensured a good 7×7 reconstruction proved by the sharp 7×7 LEED pattern.

The deposition of high purity (99.999%) aluminum and magnesium was realized with the use of home-made [76] water-cooled Knudsen cells. The two evaporators were mounted in the same plane, at an angle of 60° between them. The co-deposition took place with the sample face pointing towards the middle of the displacement angle, i.e. 30° . Thermocouples were spring-loaded to the crucible for temperature read-out and deposition rate control. The deposition rates were determined by a quartz micro-balance attached to the manipulator. The readings of the rate were made with the head of the micro-balance in front of the evaporators and multiplied by $\cos 30^\circ$.

A further correction for the determination of the deposition rate of both metals is needed because of the different definition of ML for the two elements: if we define 1 ML as constituted by N_0 atoms, it will correspond to $1.271 \times 10^{19} \text{atoms}/\text{m}^2$ in the case of Mg grown in the (0001) direction, and to $1.412 \times 10^{19} \text{atoms}/\text{m}^2$ in the case of Al(111), depending on the different in-plane lattice constants for the two elements; therefore we have to correct the value obtained by the calibrations and refer the ML unit of the alloys to that of pure Al^2 .

The evaporations were performed on substrates cooled to liquid nitrogen temperature to make the reaction at the interface weak enough to avoid silicide formation. It has been observed by Aballe [64] that the highly reactive

²This means that 1 ML of Mg correspond to 0.9 ML of Al. Note that the definition depends on the structure parameters of the films which, depending on the alloy composition, can vary strongly. We have decided, for simplicity, to refer always to the definition of pure Al adding a discussion of the actual implication of such decision where it could give confusion.

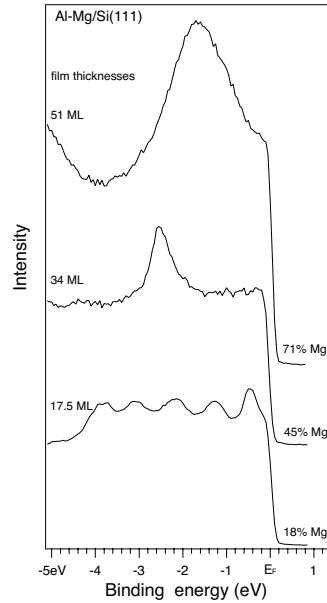


Figure 5.7: Photoemission spectra of three Al-Mg alloy compositions: the Al-rich composition presents intensity modulations typical of QWS; the Mg-rich only a broad feature and the intermediate composition a huge peak with some modulation on both sides.

systems Al/Si and Mg/Si can produce sharp interfaces just by lowering the temperature of the substrate.

5.4 Experimental results: ARUPS

In Fig. 5.7 three representative photoemission spectra are shown, taken at normal emission for three alloys of different compositions and thicknesses. All spectra are normalized to the photon flux measured on the last mirror of the beamline. The differences between the three spectra are clear: for the Al-rich alloy the spectrum is similar to that of the Al/Si system, while the Mg-rich alloy spectrum is completely different and presents only one broad peak. The spectrum relative to the intermediate composition shows a large peak and some possible modulation on the low binding energy side. The compositions of the three alloys correspond to the three regions of the phase diagram for the Al-Mg system (see fig. 5.1), and it is therefore reasonable to divide the results into three groups corresponding to these three regions.

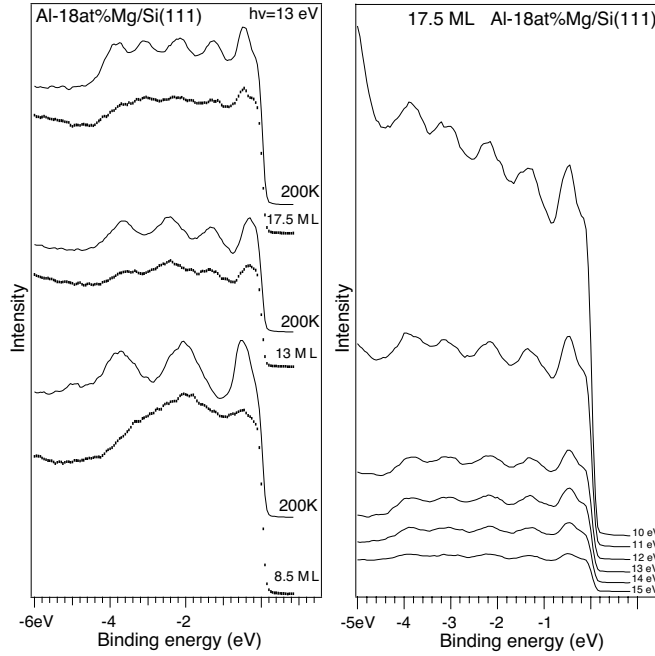


Figure 5.8: Photoemission spectra at normal emission of the Al-18at%Mg alloy. (left) Dotted lines are for spectra taken after a new deposition and continuous lines after annealing at 200K; (right) spectra taken at different photon energies. The peak positions do not change with photon energy, i.e. peaks have localized nature.

Al-rich alloys

Spectra recorded in normal emission from films of various thickness of an Al-18at%Mg alloy (Mg atomic concentration is 18%) are plotted in Fig. 5.8. Dotted lines correspond to the spectra taken just after a new low-temperature deposition (at $\sim 100\text{K}$) while the continuous lines correspond to spectra after annealing at $\sim 200\text{K}$ for 5 minutes. The effect of annealing is to order the films. Especially in the very thin ones, the formation of the surface state is obtained only upon annealing. The identification of the surface state and the QWS is clear by looking at the differences for the three thicknesses: the peak at $\sim 4\text{ eV}$ binding energy does not shift by further deposition, while the other peaks do and their number increases as well.

By varying the photon energy between 10 eV and 15 eV the peaks do not

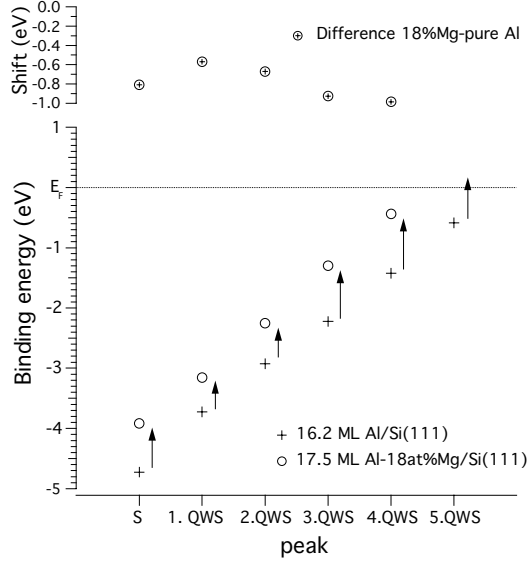


Figure 5.9: Surface state (S) and quantum well state (QWS) binding energy in the 18at%Mg alloy and in the pure Al and their shift.

shift as can be seen on the right side of Fig. 5.8, i.e. they do not disperse with k_{\perp} . In Fig. 5.9 we show a comparison of the growth of this alloy with that of pure aluminum (*cf.* Fig.5.6 with Fig. 5.8). The surface state is shifted towards lower binding energies and for the thickest film the shift reaches a value of about 0.8 eV (nearer to the Mg surface state). The QWS are shifted in the same direction, and for the almost identical thickness the number of QWS below the Fermi edge is one less. Also, the dependence of the number of QWS on the thickness is different. For our alloy there is a new QWS every ~ 4 ML while for Al it occurs every ~ 3 ML.

To understand the shift of the surface state due to alloy formation, we can refer to the theory of Schlüter and Varma where the substitution of the Fermi level of pure Al with an averaged \bar{E}_F has been analyzed via VCA. The adoption of this theory means to assume that the 18at%Mg alloy corresponds to a metal with NFE character similar to pure aluminum, but with different charge density \mathbf{n} . This charge density is averaged over the alloy film:

$$n_c^* = n_{Mg}(c) + n_{Al}(1 - c) \quad (5.6)$$

where n_c^* represents the effective charge density for the alloy of Mg atomic concentration c . In the free electron model, the electrons occupy states of increasing energy from the bottom of the spectrum up to the Fermi level

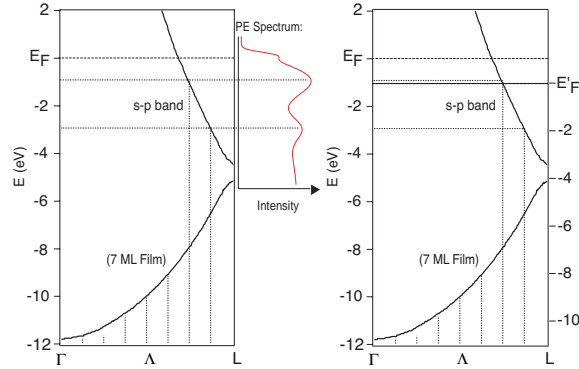


Figure 5.10: Band structure of Al [63] in the Γ -L direction. (left) 7 ML Al/Si(111) case: the discretization is revealed by the existence of peaks in photoemission spectra. (right) The band structure of Al-18at%Mg is presumed to be similar to that of pure Al. The Fermi level is lowered because of the different charge density. In this case of 7 ML, the second quantum well, which in the case of pure Al has a binding energy ~ 0.7 eV, in the case of the alloy stays above the Fermi level and is, therefore, not visible in photoemission.

E_F where all the electrons are accommodated. This value depends on the charge density through:

$$E_F = \frac{\hbar^2}{2m} \sqrt[3]{(3\pi^2 n)^2}. \quad (5.7)$$

In the case of Mg, the charge density is $8.6 \times 10^{28} m^{-3}$ corresponding to the Fermi level at 7.12 eV, while for the Al the charge density is $18.07 \times 10^{28} m^{-3}$ and E_F is at 11.66 eV [1]. If we now calculate the value of the Fermi level in the case of $c=0.18$ we obtain $n_c^* = 16.4 \times 10^{28} m^{-3}$ and $E_F = 10.9$ eV, i.e. almost 0.8 eV lower than the Fermi edge of aluminum. This value is almost exactly the shift of the surface state with respect to the Fermi edge that we have observed, showing that this interpretation of our data gives already a good result.

In Fig. 5.10 the fundamental idea of our model is represented: the effect of varying the charge density of the alloy system results in a variation of the Fermi level with respect to the bottom of the spectrum, so that the bands are rigidly shifted towards lower binding energies.

Looking at the phase diagram in Fig. 5.1 it may be thought that the Al-18at%Mg alloy is given by a coexistence of the two stable phases named α and β , where the α phase is the pure aluminum and the β , also called β -Mg₂Al₃, has a very complex fcc structure with 1,173 atoms per unit cell

and a lattice constant $a=28.22 \text{ \AA}$.

Van Agterveld [72], who studied the Al-Mg alloys with local probe scanning Auger and scanning electron microscopy (SAM and SEM), showed that in the case of bulk alloys with a concentration of magnesium of 20%, Mg segregates to the surface where there is formation of a texture of branched and dendritic disordered features. So the surface of such alloys presents areas with different magnesium concentration.

On the other hand, the density of states is an average quantity, thus the possible presence of two phases does not change the interpretation of our results, it may give rise to a superposition of spectra. Anyway, this is not observed in our spectra, showing that the annealing temperature (about 200K) is still very low for the formation of separate phases and the result is a metastable alloy which has a 18at% Mg concentration throughout the film.

The alloying process also produces other effects, for example a change of lattice constant is expected when Mg atoms are introduced in the array of Al, due to the difference in the atomic radii of the two elements: the value of r_S for Mg is higher than that of Al³. The increase of the lattice constant corresponds to a decrease of the Brillouin zone in reciprocal space and then a possible shift of the surface state. The gap is formed by the Bragg reflection of the electron wavefunction at the border of the BZ, hence if the BZ is smaller, the gap has a shift towards higher binding energies, i.e. in a direction contrary to the shift we have observed.

It has been demonstrated that the lattice constant increases by 0.0047 \AA per at%Mg [77], producing in the case of 18at% of magnesium an increase of the lattice constant of about 3%, with a correspondent shift of the gap of about 0.1 eV towards higher binding energy.

One more quantity influenced by the alloying process is the work function Φ . This affects the surface state binding energy, as predicted by Smith [74], with calculations made within the phase accumulation model framework and observed by Neuhold and Horn [78] in the case of Ag. The change in this case was $\sim 20\%$ of the work function change. In our case the work function of Mg and Al is 3.6 eV and 4.2 eV respectively, so, at maximum a change

³ $r_S^{Mg} = 2.6$, $r_S^{Al} = 2.07$. r_S changes depending on the concentration of the alloy and then changes the lattice constant, in fact, the value of r_S is approximately the value of the interatomic spacing in nearest-neighbour pairs.

of 0.6 eV is possible leading to at maximum a shift of ~ 0.1 eV. In the case of $c=0.18$, and assuming a linear change of the work function with Mg concentration the shift should be about 20 meV.

All these considerations are in agreement with our results and may explain some discrepancy between the VCA predictions (without considering other effects) and the experimental observations.

Photoemission spectroscopy is particularly useful in studying the dispersion $E(k)$ of the bulk and surface bands, when applied in the angle resolved mode. By recording spectra at various emission angles it is possible to obtain the dispersion making use of the relation between k and the emission angle θ_e :

$$|\mathbf{k}_{\parallel}| = \sin \theta \cdot \sqrt{\frac{2mE_{kin}}{\hbar^2}}. \quad (5.8)$$

Fig.5.11(a) shows a collection of spectra taken with $\hbar\omega=13$ eV at various

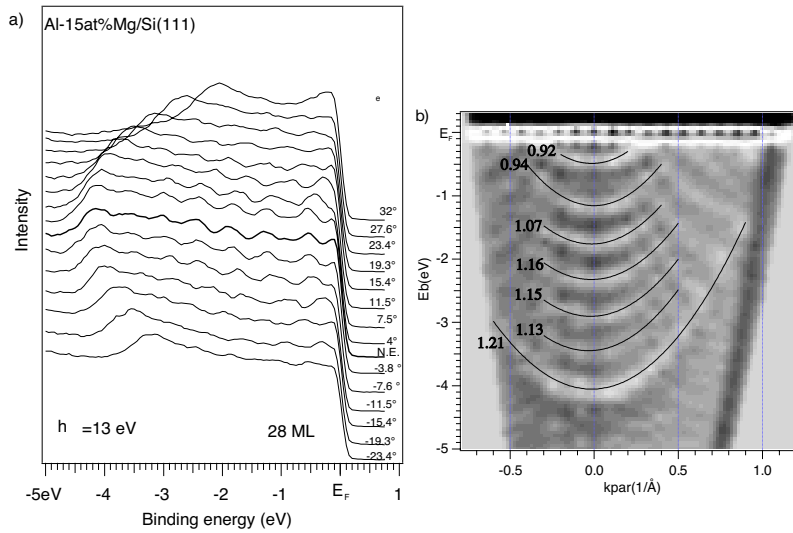


Figure 5.11: (a) Photoemission spectra taken at various emission angles of the 15at% Mg alloy. (b) Gray scale intensity plot of the 15at% Mg alloy. The lines represent the parabolic fit. The values of m^*/m_e are also reported.

emission angles on a 28 ML thick film of a Al-15at%Mg alloy. It is obvious that the seven peaks, present in normal emission, disperse with emission angle. The same spectra are also presented in a gray scale representation,

where the second derivative of the photoemission intensity is plotted (Fig. 5.11(b)). In this figure the brightest points correspond to the peaks; in this way it is easier to follow the peaks in the first BZ up to $\sim 1.1 \text{ \AA}^{-1}$. Also presented are the parabolic fits of the in-plane dispersion of the surface state and the QWS, which visibly present a parabolic dispersion and can be therefore characterized in terms of an effective mass m^* where $E_b = \frac{\hbar^2 k^2}{2m^*}$. The result of the fit for the surface state gives a value of $\frac{m^*}{m_e} = 1.21$. This value is similar to the value obtained for a 23 ML thick film of Al/Si(111) [64] showing that the introduction of Mg atoms in the Al array does not affect the scattering process because the film is made by a large ordered Al-rich phase, which gives rise to the QWS. The values of the effective masses for the dispersion of the QWS decrease in going towards the Fermi edge from $m^* = 1.13m_e$ to $m^* = 0.92m_e$.

Intermediate composition alloys

In the intermediate concentration, $0.32 \leq c \leq 0.55$ there is another problem to deal with, given by the instability of the structure in this composition range. In the bulk, at $\sim 38\text{at}\% \text{Mg}$ there is the transition to the β phase, at $\sim 42\text{at}\% \text{Mg}$ to the β' phase and at $\sim 55\text{at}\% \text{Mg}$ the γ phase. Fig. 5.12 shows

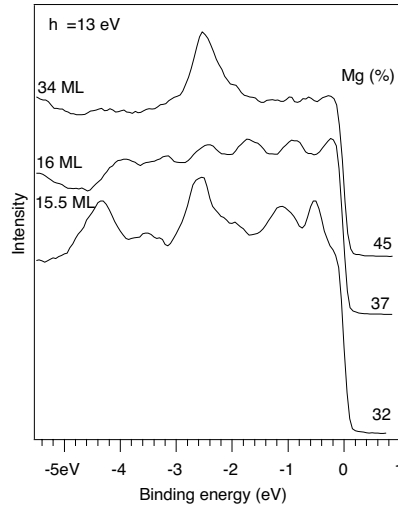


Figure 5.12: Photoemission spectra taken at normal emission of alloys with intermediate composition.

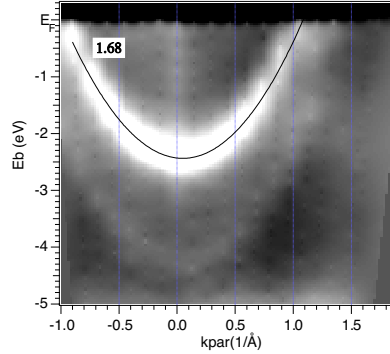


Figure 5.13: Gray scale direct intensity plot of the 45at%Mg alloy. The number is the m^*/m_e values obtained by the parabolic fit (black line). At higher binding energy a peak dispersing with NFE character is observed.

spectra of alloys in the range 32-47at%Mg for various thicknesses and preparation procedures. These three spectra look very different, and especially the one for the Al-32at%Mg is very complicated. As in the other alloys, all the peaks are stationary with photon energy (not shown). In the case of the Al-32at%Mg, the spectrum is made up of an overlap of two different features, one of which gives the more intense peaks at -4.35 eV, -2.6 eV and -1.1 eV, while the other one gives the broader and less intense peaks at -3.5 eV, -2 eV and -0.5 eV. Also in the spectrum from the 37at%Mg there is a similarity with the first one: in this case the peaks are located at -3.95 eV, -2.45 eV, and -0.9 eV, and at -3.26 eV, -1.7 eV, but in this case all have similar intensity. The film of the Al-32at%Mg alloy has been obtained after a deposition of about 15 ML at 100K and subsequent annealing to RT, while for annealing at lower temperatures the film presented only broader features (not shown). The 45at%Mg alloy has a large peak at -2.45 eV. This spectrum has been also obtained just after a prolonged annealing at room temperature, with a broad feature at lower temperature. This seems to be typical of the alloys in this range of composition.

As is clear from Fig. 5.12, a shift of the surface state with respect to the Fermi level is produced by the alloying process. This shift, due to the decrease of the density of states, should give the values $\delta E_F = 1.33, 1.55$ and 1.9 eV, for the three alloys with 32at%, 37at% and 45at%Mg⁴, respectively. However, the apparent surface state shifts in these three cases are: 0.4, 0.5 and 2 eV, and therefore much less than the predicted ones, with the exception of the Al-45at%Mg alloy. This means that in this region of the phase

⁴In the case of 32at%Mg and 37at%Mg the shift is referred to the first set of peaks, being more intense, while for the 45at%Mg, the reference is the large peak.

diagram, the VCA cannot be used in its simple formulation.

For the alloys considered here phase separation occurs, and both phases contribute to the spectra. This happens clearly in Al-32at%Mg and Al-37at%Mg, giving rise to two sets of peaks which are very near to one another and have comparable intensity. But this happens also in Al-45at%Mg, where the two sets of peaks are more distant (in binding energy) and have different photoemission intensity, as can be seen in Fig. 5.13 where at about 4.4 eV a peak is dispersing with NFE, which also comes from a different alloy phase.

It is therefore clear that in this range of alloy composition, the separation of phases is very efficient and both alloy phases contribute to the photoemission spectra, and both present band discretization and a surface state.

It has to be noted that, if the two phases are connected, the Fermi level has to be the same, and is determined by the average of the charge density present in the two phases, although every phase has a different charge density because of the different composition. The fact that we observe surface states with different binding energy tells us that the thin film has patches of different alloy phases which behave as independent systems. The formation of unconnected phases is reasonable if we observe that the order and formation of discrete electronic bands is obtained only after an anneal at relatively high temperature. The intensity of the two sets of peaks is related to the lateral extension of the patches; by increasing the Mg content in the alloy, the peaks from the phase with more Mg (with peaks at lower binding energy) become more intense.

Mg-rich alloys

An example of a Mg-rich alloy is given in Fig. 5.14(a) where the growth of a Al-71at%Mg alloy is shown. The photoemission spectra are dominated by a broad peak at about 1.5 eV. The variation of photon energy does not affect the binding energy of this feature, making clear that it has a localized nature (see Fig. 5.14(b)). Also for this composition the prediction of the rigid band model can be tested by comparing the Fermi edge shift with the shift of the surface state with respect to the Fermi edge. The δE_F is in this case 3.1 eV, predicting a surface state at about 1.55 eV, very near to the position of the broad peak in Fig. 5.14. The presence of a broad peak is

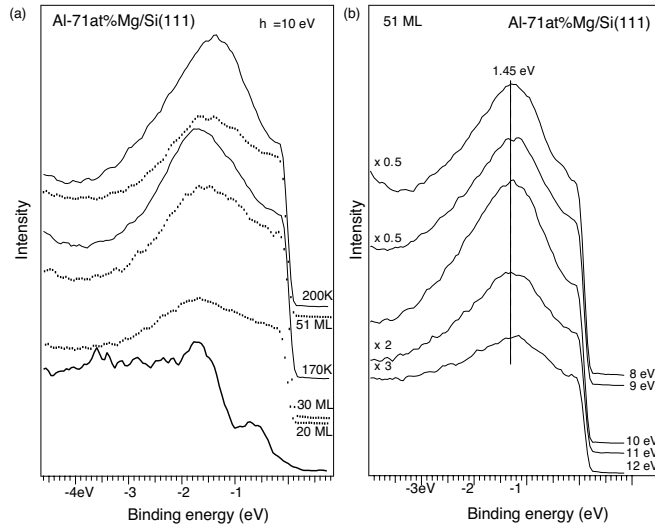


Figure 5.14: (a) Photoemission spectra taken at 10 eV of as deposited (dotted lines) film and after annealing (continous lines). (b) Spectra taken at various photon energies show the localized character of the peak.

likely to be the result of the two phases present in this range, which are the γ -AlMg with fcc structure and the hcp Mg-rich phase (see phase diagram). It is clear that these phases are more disordered than the Al-rich ones and therefore, the band discretization is not efficient. From this point of view, the Mg-rich alloys are less interesting. Moreover, upon increasing the Mg content, the VCA should not work anymore because of the transition to the hcp structure. In fact, the value of the surface state energy in pure magnesium is 1.65 eV [65], higher than that found in the Al-71at%Mg alloy. The broadness of the peak we have found could, therefore, be due to the existence of two narrower peaks, one due to the hcp phase with high Mg content and one with less magnesium and with a fcc structure.

5.5 Collective excitations in simple metals and alloys

In the previous sections it has been shown that the Al-Mg alloy results in nearly free electron (NFE) systems with an average charge density and average properties over a wide range of composition. For these systems it is,

therefore, possible to refer to the jellium model to describe many electronic properties. The basic idea of the jellium model is that the lattice of positive ionic charges is replaced by a semi-infinite uniform background:

$$n_+(z) = \bar{n}\theta(-z), \quad (5.9)$$

where $\theta(z \geq 0)=1$ and $\theta(z < 0)=0$ and the only free parameter is \bar{n} , or equivalently, the average electron radius r_S introduced in the previous sections.

Among other important properties, the jellium model can be used to explain the electronic response of a metal to an incident electromagnetic field. This is a *many-body* effect and is due to collective excitations, where the electrons behave as a plasma, oscillating with the *plasmon frequency* ω_p . The dielectric function $\epsilon(\omega)$, which describes the electronic response to the external field with frequency ω , has the form $\epsilon(\omega) = 1 - (\omega_p^2/\omega^2)$. The plasmon frequency in an infinite metal in the Drude model depends on the bulk charge density n , through:

$$\omega_p = \sqrt{\frac{4\pi n e^2}{m}}. \quad (5.10)$$

Apart from the bulk plasmon excitation, the existence of a surface in a real solid introduces collective excitations due to the charges present at the surface. These are very important not only from a theoretical point of view, but also for a comprehensive understanding and the correct interpretation of all surface spectroscopies that use electromagnetic fields or charged particles. In fact, a very strong modification of both photoemission line shape and intensity has been found in various metals near their bulk plasmon frequency, which has been explained by the excitation of collective modes at the metal surface [79].

The explanation of this behaviour is related to the form of the matrix element in the photoemission process that has been introduced in the second section of this thesis. In fact, if the spatial variations of the photon field $\nabla \cdot \mathbf{A}$ are neglected, the matrix element M_{ij} in the Fermi's golden rule:

$$j(\mathbf{R}, E, \hbar\omega) \propto \sum_{i \text{ occup}} |\langle \Phi_i^* | \mathbf{A} \cdot \mathbf{p} + \mathbf{p} \cdot \mathbf{A} | \Phi_i \rangle|^2 \delta(E_i - \hbar\omega - E_f) \quad (5.11)$$

can be assumed to be:

$$M_{ij} \propto \mathbf{A}_0 \langle \phi_f | \nabla \mathbf{V} | \phi_i \rangle \quad (5.12)$$

where \mathbf{V} is the potential felt by the electrons. For photon energies commonly used in a photoemission experiment, for example 20 eV, the wavelength is 50 nm, i.e. large compared to the atomic distances, and the assumption $\nabla \cdot \mathbf{A}=0$ is correct. However, for photon energies near the collective excitations the response of the metal electron to the electromagnetic field cannot be neglected, since it causes the fluctuation of the charge density in the surface region, leading to strong variations of the vector potential \mathbf{A} . Hence the initial assumption becomes $\nabla \cdot \mathbf{A} \neq 0$, and the exact solution of the equation (5.11) requires a calculation of the effective electromagnetic field in this region. The theoretical and experimental proof of the importance of the response to the incident field has been given by Levinson *et al.* [80], who observed a strong enhancement of the photoyield at about $0.8 \omega_p$ and attributed it to the $\nabla \cdot \mathbf{A}$ term on the basis of self-consistent field calculations within the random-phase-approximation (RPA).

In classical terms, the solid, represented by the frequency dependent dielectric constant $\epsilon(\omega)$, is separated from the vacuum by an infinitely sharp boundary. Maxwell's equations give a continuous radiation field in the direction parallel to the surface and a discontinuity of the perpendicular component of the transverse field when $\epsilon(\omega) \neq 1$.

The resulting charge density n is described by a delta function sheet in the surface plane $\mathbf{n}(\mathbf{r}, \omega) = e^{i\mathbf{q}_{\parallel}\mathbf{r}_{\parallel}}\phi(z, \omega)$ where \mathbf{q}_{\parallel} is the wave vector parallel to the surface. This fluctuating surface charge has dipolar character along the plane of the surface because the metal surface remains neutral. Hence the resulting electric field varies continuously in the direction parallel to the surface and has a discontinuity in the direction perpendicular to the surface: $E_z(z = 0^{\pm}) \propto \mp q_z$.

Considering the vacuum described by a dielectric constant $\epsilon_0=1$, the discontinuity of the electric field can be written as $\epsilon(\omega)E_z(0^-) = E_z(0^+)$, which implies $\epsilon(\omega)=-1$. As mentioned above, the Drude model of an infinite metal gives $\epsilon(\omega) = 1 - (\omega_p^2/\omega^2)$, so, considering the abrupt boundary with the vacuum, a *surface plasmon* results whose frequency $\omega_s = \omega_p/\sqrt{2}$, is dependent on the bulk property ω_p (and is hence not a surface property).

This result, derived from the assumption of an abrupt charge density profile, is certainly far from being realistic. Bennett [81] attempted to take into account a charge distribution across the surface, and calculated the electronic response to a linearly decreasing charge density through a surface

region from the bulk value to zero, using a simple hydrodynamic model. For a sufficiently diffuse electron charge at the surface, he observed additional plasmon modes.

Contrarily to the “classical” surface excitation, which is monopolar (i.e. the charge distribution has a simple peak in the direction z) the new modes have multipole character and have a frequency between those of the surface and the bulk plasmon. It is easy to imagine that the next step for obtaining more complex plasmon modes is to describe the charge density profile at the surface of a metal in a better way, and this means to use the ground-state charge distribution of a jellium-like surface calculated by Lang and Kohn [82] within the local density approximation (LDA).

Here, because of the sharp cutoff of the electronic wave vector at the Fermi surface, the charge density presents decaying Friedel oscillations in the bulk side with wavelength $\pi/k_F=1.64 r_S$. On the vacuum side, the charge density has the form:

$$n(z) = \bar{n} \left[1 + \frac{a \cos(2k_F z + \alpha)}{z^2} + \dots \right], \quad (5.13)$$

where a and α depend on the shape of the surface potential [82]. Also here the actual profile depends on the parameter r_S through the k_F value. In Fig. 5.15(a) the LDA profiles for two r_S values are shown.

It should be also noted that the classical field, due to the charge density induced by the external electromagnetic field, does not consider the effect of the dynamical screening due to the charge near the surface. The fields in the vicinity of the surface have to be calculated self-consistently by taking the response of the electron density into account. The single particle wavefunctions for the ground state description of the solid are used, and the many-body screening aspects of the response are put into an “effective” field [83],[84].

Hence, due to the dynamical screening of the external field, the surface electromagnetic field varies rapidly and deviates appreciably from the classical Fresnel field, as shown schematically in Fig. 5.15(b), where the dashed line indicates the classical (Fresnel) field and the solid curve indicates the microscopic field. Beyond z_1 and z_2 are the asymptotic regions where the classical description is adequate. The main feature of the microscopic surface field is the smooth variation between bulk and vacuum, and the displacement of the effective surface [84]. This dielectric response is a manifestation of

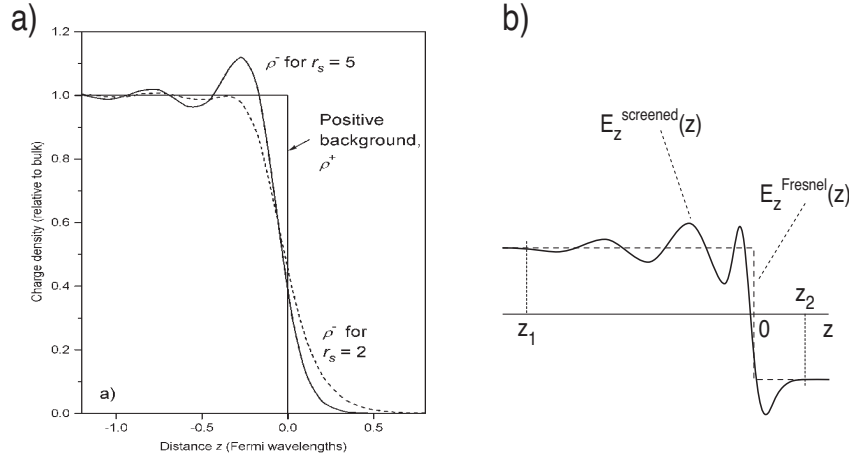


Figure 5.15: (a) Ground-state charge distribution obtained by Lang and Kohn for jellium-like surfaces with two different values of r_s . (b) Comparison of the Fresnel and the microscopic field (from ref. [84]).

many-body effects, leading to the large differences between the screened field and the incident field. The oscillations of the charge profile at the surface set up longitudinal fields. The field enhancement is connected with the new collective mode of the electron gas at the surface. This is the mode predicted by Bennett [81] for the linear charge profile (see Fig. 5.16(a)).

For a metal-adlayer system, Inglesfeld and Wikborg [85] found a charge density profile resembling that described in Fig. 5.15(a) for a clean metal surface, obtaining, within the RPA framework, a surface multipole excitation. More recently, the understanding of collective excitations on both clean metal surfaces and alkali adlayers has made great progress, by introducing the study of such systems within the jellium based time dependent local density approximation (TDLDA) [86],[87].

In this way, Liebsch found the existence of an adlayer multipole plasmon which is related to the formation of a well-defined charge density plateau corresponding to the alkali-metal adlayer. This new feature has been identified with a bulk-like plasma oscillation but is not present in the bulk samples. It is rather similar to a surface plasmon and is due to the confinement of the charge along the direction normal to the film growth, for this reason and because of the smoothness of the charge variation through the interface, the frequency of this plasmon is slightly different from the bulk plasmon. The

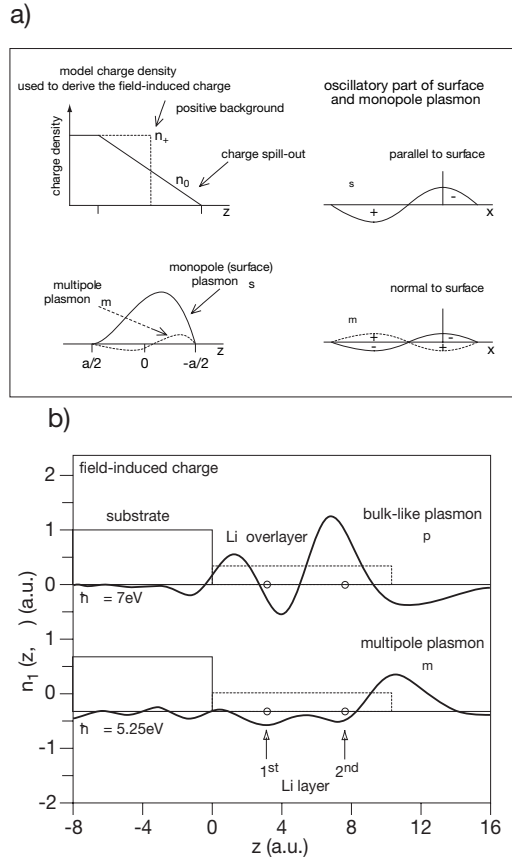


Figure 5.16: (a) Representation of the multipole plasmon made by Inglesfeld and Wikborg with a linear charge-density profile. (b) TDLDA calculations of the charge induced in a 2 ML Li/Al film. For this thickness the bulk-like plasmon is stronger than the multipole. By increasing the thickness, the confinement of charge in the bulk-like plasmon is less efficient and it becomes weaker. From this picture it can be noted the localized nature of the multipole plasmon.

field induced charge density for a 2 ML thin Li film on Al substrate is shown in Fig. 5.16(b), for both multipole and bulk-like plasmon.

Since the thin films exhibit both the multipole surface and the bulk-like plasmon excitation, one can examine the relative strength of these excitations and the influence of the film and the substrate on these modes. Thin films of alkali metals like Na, K, and Li deposited on Al have been object of many of such studies, where the changes in frequency, full width at half maximum (FWHM), and intensity of the alkali collective excitations as a function of smooth adlayer coverage are investigated [88] by means of photoemission spectroscopy.

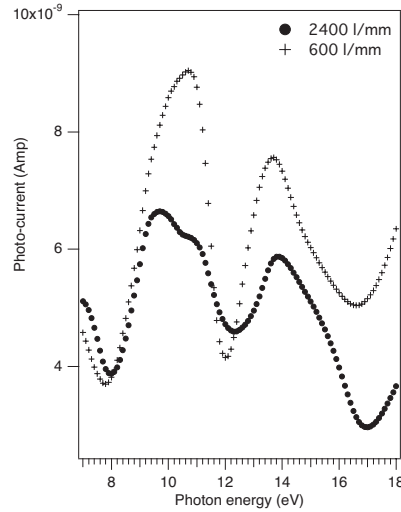


Figure 5.17: Beamline photoyields obtained by measuring the photo-current on a GaAsP diode, with two different gratings. The flux is then normalized by the diode photoyield and by the ring current to take into account also its natural decreasing with time.

5.5.1 Experimental results: CIS spectroscopy

Photoemission spectroscopy is capable to detect both the bulk-like (in thin films) and the multipole plasmons, while bulk and surface plasmons at $q=0$ cannot be excited by the electromagnetic waves, because of their monopolar character. This gives a great advantage for detecting the multipole and bulk-like plasmons because the spectra are not overloaded by the real bulk and surface plasmons, as happens in the case of Electron Energy Loss Spectroscopy (EELS). In order to measure the yield of photoelectrons as a function of photon energy, the Constant Initial State (CIS) mode is used, meaning that both the photon energy and the analyzer energy are moved in parallel so that the signal is always taken from the same initial state. In all the following CIS spectra, states near the Fermi level (about -0.3 eV binding energy) have been chosen.

The spectra are then normalized by the beamline flux curve that depends on the monochromator characteristics and can be obtained in two ways: by measuring the photocurrent on the last mirror of the beamline or by introducing a photodiode between the last mirror of the beamline and the sample, measuring in this way the beamline flux. The first case allows us to measure the CIS spectrum and normalizing flux at the same time, on the other hand, the use of the photodiode resulted in a more efficient method, giving a precise beamline photoyield.

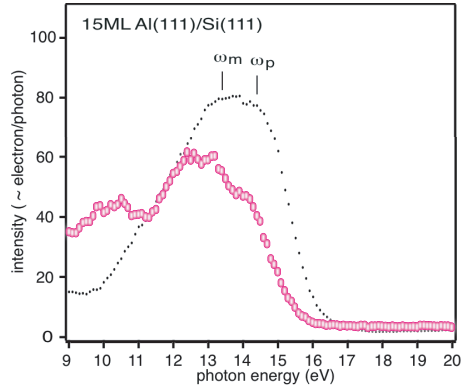


Figure 5.18: CIS spectra of a 18 ML and a 15 ML thin film of Al/Si(111) measured on two different beamlines: 3m-NIM (open circles) and 1m-Seya Namioka (dots, from ref. [64]). The different monochromators used in the two experiments are responsible for the different shape of the spectra. In fact, the peaks observed in the 3m-NIM spectrum at about 10 and 12 eV are due to the normalization.

In Fig. 5.17 we show the beamline photoyield after normalization with the flux obtained from the GaAsP diode, for two different gratings. As is clear from the plot, the 3m-NIM monochromator has a very complex photoyield with intense maxima and deep minima in the energy range where plasmons are expected for our system. This means that the shape of the beamline photoyield can introduce unphysical features in the measurement of the CIS spectra. To check this possibility we measured the CIS spectra for the pure Al/Si system and compared it with previous measurements.

In Fig. 5.18 we report two spectra of a 15 ML Al/Si(111) thin film. Our spectrum, measured on the 3m-NIM beamline with the 2400 l/mm grating, has four peaks at ~ 10 eV, 12.4 eV, 13 eV and 14.1 eV. The reference spectrum has been measured on the 1m-Seya Namioka beamline at Bessy I (from ref. [64]) and has two peaks at 13.1 eV and 14.4 eV, assigned to the adlayer multipole surface plasmon and bulk-like plasmon, respectively. Hence it is clear that the normalization introduces artifacts in the spectra.

This is very important when the expected plasmon peaks have lower energy, like in the case of Mg. In fact, magnesium has a lower charge density than aluminum and has therefore a lower plasmon energy, i.e. 11 eV [1]. The multipole surface plasmon is expected at ~ 9 eV, in the spectrum region where the monochromator introduces a systematic error. This is evident in

Figure 5.19: CIS spectrum of a 27 ML thin film of Mg/Si(111). The bulk-like (ω_p) and the multipole (ω_m) plasmon are respectively at ~ 11 eV and ~ 9.5 eV. In this spectrum they are very weak shoulder of the more intense peak at 8.5 eV due to the normalization.

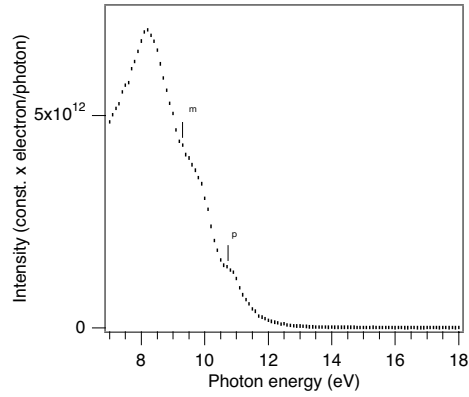


Figure 5.20: Photoyield of two Mg/Si(111) thin films, measured on the 3m-NIM beamline with the 600 l/mm grating. The relative intensity of the two plasmons depends strongly on the thickness of the film, because the bulk-like plasmon (ω_p) depends on the confinement of the charge in the thin film.

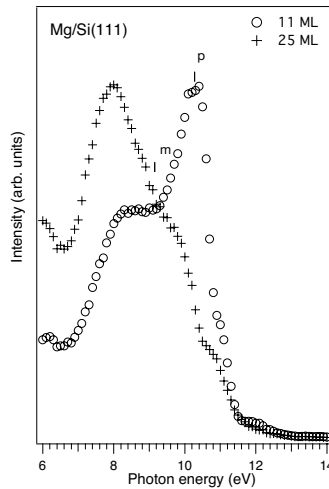


Fig. 5.19 where a 27 ML Mg/Si(111) thin film is shown.

To overcome the problem of flux normalization on the 3m-NIM beamline, we have performed the same experiments on another beamline, the TGM-4 for which the toroidal grating monochromator offers a more regular photoyield in the energy range of interest. Although the lowest photon energy that can be reached with the TGM-4 monochromator is only 10 eV, for the purpose of studying the collective excitation the use of this monochromator has been preferred because in the energy range between 10 eV and 15 eV the monochromator has a monotonous photoyield.

As seen from the ARUPS experiments, alloy formation leads to the variation of the charge density of the system, with consequences on the surface state

and the quantum well states position. Also the bulk plasmon frequency depends on the averaged value of the charge density (see equation (5.10)). Thus, alloys with different charge density values may present distinct collective excitations in the photon energy range between the plasmon frequencies of magnesium ω_{Mg} and aluminum ω_{Al} .

In addition, analyzing the relative intensity of the multipole and the bulk-like plasmon in CIS spectra, it is possible to obtain informations on the nature of these collective excitations, especially when comparing thin films of different thickness, like in Fig. 5.20. As it is clear, the relative intensity is strongly dependent on the thickness and the ratio between the bulk-like and the multipole plasmon decreases as the thickness increases.

To understand the reasons for this behaviour, one has to consider that the multipole surface plasmon is given by the charge density at the surface and it depends on the screening property of the surface electrons only, i.e. it is *localized* on the surface. On the contrary, the bulk-like plasmon is due to the confinement of the charge in the entire thin film and it has a more *de-localized* nature (see Fig. 5.16(b)). The latter excitation is, therefore, very important for very thin films, where the confinement is on a small region, and its intensity decreases for thicker films.

By simulating the experimental CIS spectra of Al-13at%Mg/Si(111) thin films of Fig. 5.21(a), with two Voigt functions, corresponding to the bulk and the multipole plasmons, and a flat background, using a least-square minimization routine, it is possible to follow the A_p/A_m ratio as a function of film thickness (shown in Fig. 5.21(c)).

Although no theoretical calculations exist on the line shape variation of the photon-excited adlayer plasmons, we used the Voigt function because it gave better fits than either a purely Gaussian or a Lorentzian function and because it has been successfully used in other experimental studies [88]. Both Lorentzian and Gaussian components of the Voigt function line-width were varied during the fitting. A representative fit for the 7 ML thick film is shown in Fig. 5.21(b).

While the bulk-like plasmon is described by a narrow Voigt function (with a FWHM \approx 0.6 eV), the multipole plasmon has a very broad line shape with a FWHM \approx 1.2 eV. This result is not new in free-electron-metal adlayers, in fact, Barman *et al.* found a similar behaviour in the case of Li/Al, K/Al and Na/Al [88] for film thicknesses larger than 6 ML.

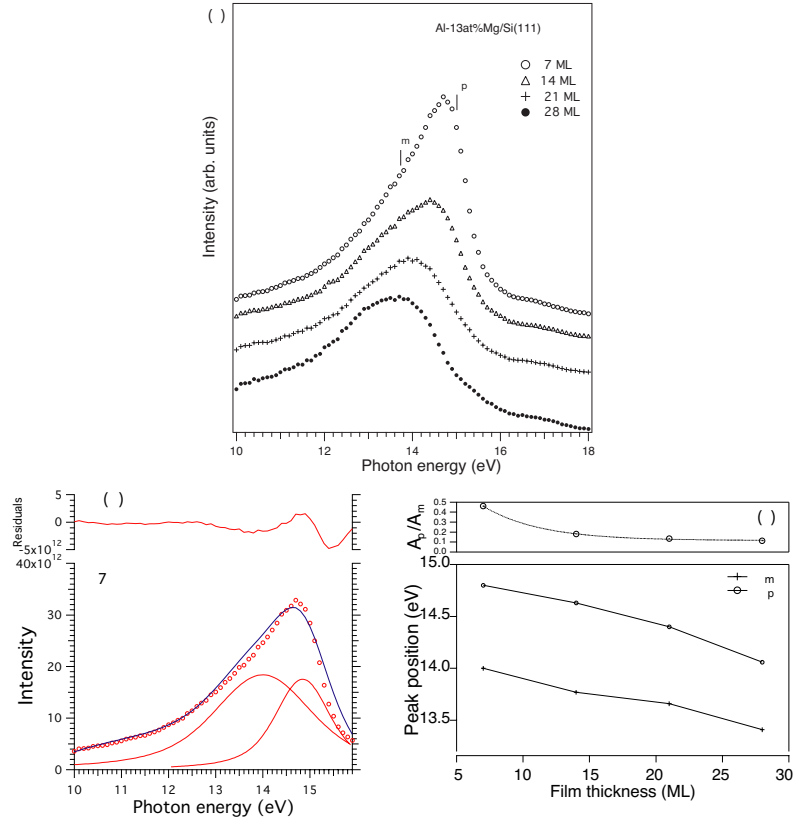
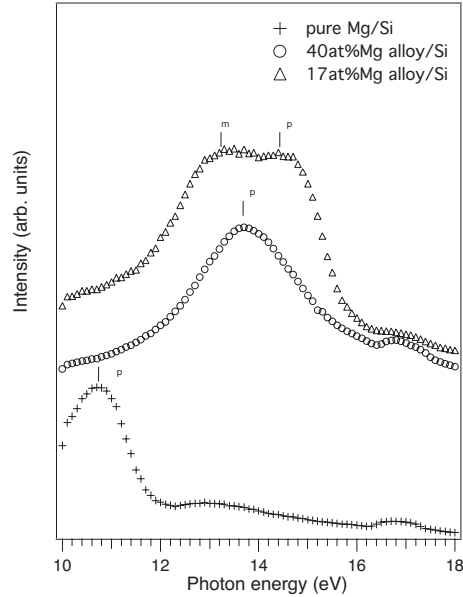


Figure 5.21: (a) Photoyield of four Al-13at%Mg/Si(111) thin films. The CIS spectra have been measured at the TGM-4 beamline, and normalized with the synchrotron ring current. By increasing the film thickness the CIS line shape changes with a decreasing of the ω_p component, which is shifted as well, and a relative increasing of the ω_m component. (b) CIS spectrum of the 7 ML thin film fitted with two Voigt functions. (c) Peak positions and ratio of areas of the multipole and bulk-like plasmon component as a function of film thickness.

The reason of the narrow bulk-like plasmon is that this mode may couple with the smooth adlayer-vacuum interface and, for relatively thick films, very weakly with the adlayer-substrate interface, with a correspondent reduction of the possible decay channels. The multipole plasmon couples with the excitations localized at the surface and, due to the high degree of localization, presents an enhanced decay with the consequent broad peak. The Al-Mg/Si system is more complex than the alkali/Al systems studied

Figure 5.22: Photoyield of three alloy thin films, measured on the TGM-4 beamline. The bulk-like plasmon (ω_p) is present in all three spectra, while the multipole plasmon (ω_m) is not distinguishable in the 40at%Mg alloy because the film is very thin and the bulk-like plasmon is very strong. In the pure Mg film the multipole plasmon is out of energy range of this monochromator.



by Barman *et al.*, because the Al-Mg alloy has a single phase only in a restricted region of the phase diagram. When the thin film is formed by two phases, a double feature, similar to what is observed in angular resolved energy distribution curve (EDC) spectra, is present, making the width of the Voigt function broader.

This is shown in Fig. 5.22, where CIS spectra from alloys with different composition are plotted. The spectrum of the 17at%Mg alloy presents two peaks easily distinguishable, at ~ 14.3 eV and ~ 13 eV; for the 40at%Mg alloy, the main peak is at ~ 13.4 eV and for the pure Mg film, the bulk-like peak is at about 10.6 eV.

From average charge density considerations, it is possible to obtain an estimate of the bulk plasmon energy. In fact, considering the charge density $n_{Al-Mg} = n_{Al} \cdot (1 - c) + n_{Mg} \cdot c$, where c represents the Mg atomic content in the alloy, and considering the dependence of ω_p on the charge density (5.10), we obtain in the two cases reported in Fig. 5.22, $\omega_p^{17\%} = 14.5$ eV and $\omega_p^{40\%} = 13.6$ eV, in very good agreement with the experimental result.

In the latter case the line shape on the high photon energy side is very different from that of a 17at%Mg alloy, showing that the peak is broader and eventually composed of two peaks corresponding to the two alloy phases.

This is not the case with the 17at%Mg alloy, where only one phase is present, as observed in ARUPS experiments. The peak at ~ 13 eV is due to ω_m and has a ratio $\omega_m/\omega_p=0.91$.

The ratio ω_m/ω_p for free-electron-metals has values similar to 0.8 independently of the charge density and the surface [88]. The reason for this dependence is still not clear but a large body of available literature shows this coupling with a ratio varying between 0.8 and 0.89, making it an empirical result. Anyway, the ω_m/ω_p ratio from our data is higher (0.9-0.93) than those found for the alkali adlayers and this could be due to the reduction of ω_p by the core polarization effect. The multipole plasmon, on the other hand, is localized on the surface and it is therefore less influenced by the core polarization effect.

Another feature, observable from Fig. 5.21(b), is that the bulk-like plasmon shifts towards lower energy. This is related to the dispersion of the bulk plasmon with wave vector q and in particular with the existence of higher-order modes of the bulk plasmon, that have been predicted theoretically [89] to have a wavelength $\lambda_{\perp} = 2a/n$, where n is an odd positive number and a is the thickness of the layer, and to follow a quadratic dispersion given by

$$\omega_p(q) = \omega_p + \alpha q^2, \quad (5.14)$$

where $\alpha=0.6\epsilon_F/\omega_p$. Thus, with increasing thickness of the adlayer, the wavelength of the higher plasmon modes increases, resulting in the redshift observed in our spectra. The multipole plasmon has also a redshift with increasing thickness, and this is associated with the dependence of ω_m on ω_p .

5.6 Conclusions

We have studied thin films of Al-Mg alloys over a wide range of composition, obtained by co-depositing aluminum and magnesium on a Si(111) substrate at low temperature. The alloying process gives rise to ordered epitaxial films for the Al-rich alloys (up to 30at%Mg) and two ordered alloy phases for higher magnesium contents. These ordered systems form a surface state and discretization of the s-p bulk band due to electronic confinement, as revealed by QWS in the photoemission spectra. The binding energies of both the surface and quantum well states depend on the alloy composition.

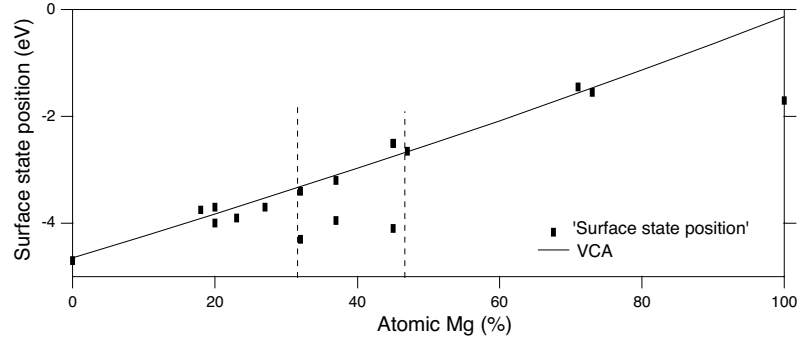


Figure 5.23: Surface state experimental binding energy (squares) as a function of the alloy composition and VCA prediction (continuous line). The prediction and the experimental data are in good agreement in most part of the phase diagram, with the exception of the alloys with composition 32-45 at%Mg, where two phases with distinct Mg content are formed. For Mg-rich alloys, the VCA is not valid, because of the different atomic structure.

The interpretation of the observed behaviour was done on the basis of the virtual crystal approximation which predicts a continuous decreasing of the charge density by increasing the Mg content in the alloy. In Fig. 5.23 we summarize the experimental data and the VCA prediction for the surface state binding energy. As is clear, the binding energy very closely follows the VCA prediction, with the only exception in the intermediate alloy compositions, where the phase separation leads to two peaks, one at higher binding energy and the other one at lower binding energy, similar to the predicted one. The alloys with higher Mg content form a surface state, although the relative phases should be very disordered. Their binding energy is also very close to that predicted by the VCA, showing that this is related only to the alloy composition. These results indicate a strong similarity with the behaviour of Al-doped MgB_2 and show that the electronic properties of these materials can be tailored by the actual composition in a relatively smooth way.

The study of collective excitations in these alloys reveals also an interesting behaviour of both bulk-like and surface plasmons, with a direct proportionality of plasmon energy to the actual composition of the alloys. This is in agreement with the nature of both excitations where their behaviour is dominated by the charge profile in the surface region and at the interface and therefore, is strongly related with the r_s value of the system. Anyway, the

existence of two alloy phases in thin films of particular compositions results in broad peaks where two components are present.

